

High-order discontinuous Galerkin nonlocal transport and energy equations scheme for radiation hydrodynamics

M. Holec^{1,2,*}, J. Limpouch², R. Liska² and S. Weber¹

¹*Eli-Beamlines Institute of Physics, AS CR, v.v.i, Na Slovance 2, 180 00 Prague 8, Czech Republic*

²*Faculty of Nuclear Sciences and Physical Engineering, Czech Technical University in Prague, Brehova 7, 115 19 Prague 1, Czech Republic*

SUMMARY

The nonlocal theory of the radiative energy transport in laser-heated plasmas of arbitrary ratio of the characteristic inhomogeneity scale length to the photon mean free paths is applied to define the closure relations of a hydrodynamic system. The corresponding transport phenomena cannot be described accurately using the Chapman–Enskog approach, that is, with the usual fluid approach dealing only with local values and derivatives. Thus, we directly solve the photon transport equation allowing one to take into account the effect of long-range photon transport. The proposed approach is based on the Bhatnagar–Gross–Krook collision operator using the photon mean free path as a unique parameter. Such an approach delivers a calculation efficiency and an inherent coupling of radiation to the fluid plasma parameters in an implicit way and directly incorporates nonequilibrium physics present under the condition of intense laser energy deposition due to inverse bremsstrahlung. In combination with a higher order discontinuous Galerkin scheme of the transport equation, the solution obeys both limiting cases, that is, the local diffusion asymptotic usually present in radiation hydrodynamics models and the collisionless transport asymptotic of free-streaming photons. In other words, we can analyze the radiation transport closure for radiation hydrodynamics and how it behaves when deviating from the conditions of validity of Chapman–Enskog method, which is demonstrated in the case of exact steady transport and approximate multigroup diffusion numerical tests. As an application, we present simulation results of intense laser-target interaction, where the radiative energy transport is controlled by the mean free path of photons. Copyright © 2016 John Wiley & Sons, Ltd.

Received 15 January 2016; Revised 21 July 2016; Accepted 31 July 2016

KEY WORDS: radiation hydrodynamics; nonlocal transport; Knudsen number; multigroup diffusion; radiation coupling; high-order finite element method.

1. INTRODUCTION

Mankind has always relied on the necessity of sufficient energy resources. Inertial confinement fusion (ICF) is a major branch of nuclear fusion research and a possible answer to the still growing demand for energy. Almost all ICF devices to date use lasers to compress and heat fuel, which under the conditions known as Lawson criterion, would achieve self ignition. Understanding of the plasma creation process and plasma behavior then becomes attractive.

The problem of energy transport is one of the key problems needing to be resolved for successful implementation of ICF. Because most of the absorbed energy of the incident laser radiation deposition takes place near the critical density, the impact on the core region is performed by the hydrodynamic motion and by the energy transport, naturally nonlocal.

*Correspondence to: M. Holec, Faculty of Nuclear Sciences and Physical Engineering, Czech Technical University in Prague, Brehova 7, 115 19 Prague 1, Czech Republic

†E-mail: milan.holec@eli-beams.eu

In order to treat the problem of ICF, we use the model of radiation hydrodynamics where photons take the main part of the nonlocal transport of energy. The aim of this article is to use and numerically solve an appropriate radiation transport closure to the hydrodynamics equations. Such a closure should be able to handle a wide range of Knudsen number $K_n = \lambda_p/L$, where λ_p is the mean free path of photons, L the plasma inhomogeneity scale length, and K_n is the fundamental quantity characterizing the type of transport regime [1–6].

The transport regimes present in laser-heated plasmas can be divided into three regions distinguished by the Knudsen number as follows:

- $K_n \in (10^2, \infty)$ — The first region corresponds to plasma where deposition of laser energy takes place, producing high temperatures and low density of expanding plasma. This regime of transport can be named free streaming.
- $K_n \in (10^{-3}, 10^2)$ — The second region, characterized by large temperatures and densities, that are relatively not low, is typically created by the transported energy from the first region. It is typically neither opaque nor transparent. Steep gradients of temperature and density usually appear. This regime of transport can be named nonlocal transport.
- $K_n \in (0, 10^{-3})$ — The third region, represented by relatively cold and highly compressed plasma, is opaque for most of the photons. This is where Chapman–Enskog expansion method [7] applies and the regime of transport can be named diffusive.

In the first section, we write the model of radiation hydrodynamics where we use the radiation transport equation as closure. The second section is devoted to a detailed description of our DG-BGK&T numerical scheme used for modeling of the latter closure. In order to analyze numerical properties of our scheme, we show two numerical tests demonstrating the scheme capability to calculate energy transport under any condition of transport regime. Based on the one-dimensional (1D) formulation of the method, we show some simulation results of laser-target interaction in the fourth section. At the end of this work, we summarize the main aspects of our proposed method and also stress the importance of nonlocal transport in the laser-heated plasma simulations.

2. MODEL EQUATIONS OF RADIATION HYDRODYNAMICS

In the case of radiation hydrodynamics conditions created by intense laser interaction with matter, the intrinsic nonlocal transport effects characterized by the Knudsen number of photons must be considered. In order to keep the physically relevant information about the nonlocal transport, we propose the following model equations:

$$\frac{d\rho}{dt} + \rho \nabla \cdot \mathbf{u} = 0, \quad (1)$$

$$\rho \frac{d\mathbf{u}}{dt} + \nabla p = \mathbf{g}_R, \quad (2)$$

$$\rho \frac{\partial \epsilon}{\partial T} \frac{dT}{dt} + \left(p - \rho^2 \frac{\partial \epsilon}{\partial \rho} \right) \nabla \cdot \mathbf{u} = Q_{IB} - \nabla \cdot \mathbf{q} - \frac{d\epsilon_R}{dt} - \nabla \cdot \mathbf{q}_R, \quad (3)$$

where $\frac{d}{dt}$ is Lagrangian time derivative, ρ is the plasma density, \mathbf{u} the bulk plasma velocity, p the plasma pressure, T the plasma temperature, ϵ the specific internal energy density, Q_{IB} the inverse-bremsstrahlung heating of deposited laser energy density, $\mathbf{q}(T)$ is the electron heat flux defined in [8], ϵ_R the radiation energy density, \mathbf{q}_R radiation energy density flux, and \mathbf{g}_R the momentum exchange between plasma fluid and radiation. It is worth mentioning that the system earlier models conservation of mass, momentum, and total energy, which consists of specific internal, radiation, and kinetic parts, that is, $E = \rho\epsilon + \epsilon_R + \frac{1}{2}\rho|\mathbf{v}|^2$. The temperature equation (3) then includes both the specific internal energy density ϵ and radiation energy density ϵ_R evolution, that is, the whole system energy conservation. This formulation presented in [2] has an advantage in that it avoids the

usual explicit energy exchange term between plasma fluid and radiation. An explicit formula for time evolution of specific internal energy density reads

$$\frac{d\epsilon}{dt} = \frac{\partial \epsilon}{\partial T} \frac{dT}{dt} - \rho \frac{\partial \epsilon}{\partial \rho} \nabla \cdot \mathbf{u}. \quad (4)$$

The system is closed by the quantities $p(\rho, T)$, $\frac{\partial \epsilon}{\partial T}(\rho, T)$, $\frac{\partial \epsilon}{\partial \rho}(\rho, T)$ which are provided by the equation of state. The radiation related quantities are defined as

$$\varepsilon_R = \frac{1}{c} \int_{\nu} \int_{4\pi} I(\nu, \mathbf{n}) d\mathbf{n} d\nu, \quad (5)$$

$$\nabla \cdot \mathbf{q}_R = \int_{\nu} \int_{4\pi} \mathbf{n} \cdot \nabla I(\nu, \mathbf{n}) d\mathbf{n} d\nu, \quad (6)$$

$$\mathbf{g}_R = \int_{\nu} \int_{4\pi} \frac{\mathbf{n}}{\lambda_p(\nu) c} I(\nu, \mathbf{n}) d\mathbf{n} d\nu, \quad (7)$$

where c is speed of light, \mathbf{n} is direction of propagation, and ν is frequency of photons. Photon intensity I is the fundamental quantity describing radiation. Its evolution is governed by the transport equation [2]

$$\frac{1}{c} \frac{dI(\nu, \mathbf{n})}{dt} + \mathbf{n} \cdot \nabla I(\nu, \mathbf{n}) = \frac{1}{\lambda_p(\rho, T, \nu)} (S(\rho, T) - I(\nu, \mathbf{n})) \quad (8)$$

where λ_p is the photon mean free path and S is the so-called photon source function.

From the numerical point of view, Equation (8) is not easy to solve. Its discretization is very computationally demanding because of the extra angular and frequency dependence, apart from the spatial discretization. Still, it is worth doing because it provides a purely nonlocal description of radiation transport. It is also worth mentioning, that model (8) of radiation transport represents a fundamental approach to nonlocal radiation hydrodynamics closure. A nice classification of other approximate models used to close the system of hydrodynamic equations can be found in [9].

3. DISCONTINUOUS GALERKIN BHATNAGAR–GROSS–KROOK TRANSPORT AND TEMPERATURE SCHEME

This section describes the numerical method used to solve the transport and energy equations in a mutual way. In general, we can use any kind of particles appropriately described by the Bhatnagar–Gross–Krook (BGK) [5] form of the Boltzmann transport equation. Nevertheless, the method is applied to photons in our case. In general, the method is based on the discontinuous Galerkin (DG) high-order finite element discretization [10–12] in both space and angle. The scheme couples the transport part, which is the numerical solution of the BGK transport, and the energy part, which is formulated as an equation of temperature. These equations are present in the radiation hydrodynamics model as (8) and (3), respectively. Consequently, we will refer to the scheme as DG-BGK&T, where BGK stands for the transport equation and T for the temperature equation, where these are to be solved simultaneously.

3.1. Discontinuous Galerkin Bhatnagar–Gross–Krook transport scheme

The BGK form of the transport equation [2] reads

$$\frac{1}{c_p} \frac{\partial f(\mathbf{x}, \boldsymbol{\vartheta})}{\partial t} + \mathbf{n}(\boldsymbol{\vartheta}) \cdot \nabla f(\mathbf{x}, \boldsymbol{\vartheta}) = S(\mathbf{x}, \boldsymbol{\vartheta}) - k_p(\mathbf{x}) f(\mathbf{x}, \boldsymbol{\vartheta}), \quad (9)$$

where $f(\mathbf{x}, \vartheta)$ is the distribution function dependent on spatial coordinates \mathbf{x} and directional coordinates ϑ of a transported quantity, for example, photons, by the velocity c_p in the direction \mathbf{n} , that is, the transport direction. The term $S(\mathbf{x}, \vartheta)$ stands for the source of the transported quantity (particles), and $k_p(\mathbf{x})$ is the extinction coefficient equal to the inverse of the particles mean free path.

In order to find $f(\mathbf{x}, \vartheta)$ solving (9), we want to use the strong form discontinuous Galerkin variational principle on a functional space. This functional space is defined on a spatial region $\Omega_{\mathbf{x}}$ with its boundary $\Gamma_{\mathbf{x}}$ described by a set of spatial coordinates \mathbf{x} , and an angular region Ω_{ϑ} described by a set of angular coordinates ϑ . We call it a space of functions $\Psi(\mathbf{x}, \vartheta) \in H : \Omega_{\mathbf{x}} \times \Omega_{\vartheta}$. The variational form reads

$$\begin{aligned} & \int_{\Omega_{\vartheta}} \int_{\Omega_{\mathbf{x}}} \left(\frac{1}{c_p} \frac{\partial f(\mathbf{x}, \vartheta)}{\partial t} + \mathbf{n}(\vartheta) \cdot \nabla f(\mathbf{x}, \vartheta) + k_p(\mathbf{x}) f(\mathbf{x}, \vartheta) - S(\mathbf{x}, \vartheta) \right) \Psi(\mathbf{x}, \vartheta) d\Omega_{\mathbf{x}} d\Omega_{\vartheta} \\ & = \int_{\Omega_{\vartheta}} \int_{\Gamma_{\mathbf{x}}} (\mathbf{F}(\mathbf{x}, \vartheta) - \mathbf{F}(\mathbf{x}, \vartheta)^*) \cdot \mathbf{n}_{\Gamma}(\mathbf{x}) \Psi(\mathbf{x}, \vartheta) d\Gamma_{\mathbf{x}} d\Omega_{\vartheta}, \quad \forall \Psi \in H, \end{aligned} \quad (10)$$

where, in accordance with the strong DG principle, the divergence theorem was used twice, resulting in flux difference on the right-hand side. This term we use as the boundary condition of $\Omega_{\mathbf{x}}$, that is, we use the difference between the natural flux and numerical flux $(\mathbf{F}(\mathbf{x}, \vartheta) - \mathbf{F}(\mathbf{x}, \vartheta)^*)$, respectively. In our particular case of the linear transport equation, we know that the natural flux has the following form:

$$\mathbf{F}(\mathbf{x}, \vartheta) = \mathbf{n}(\vartheta) f(\mathbf{x}, \vartheta). \quad (11)$$

Because we are treating the transport of fast particles, for example, photons, we need to assure numerical stability of our method with respect to the transport velocity. That is, we choose the upwind numerical flux

$$\mathbf{F}(\mathbf{x}, \vartheta)^* = \begin{cases} \mathbf{n}(\vartheta) f(\mathbf{x}, \vartheta), & \mathbf{n}(\vartheta) \cdot \mathbf{n}_{\Gamma}(\mathbf{x}) \geq 0 \\ \mathbf{n}(\vartheta) \tilde{f}(\mathbf{x}, \vartheta), & \mathbf{n}(\vartheta) \cdot \mathbf{n}_{\Gamma}(\mathbf{x}) < 0 \end{cases}, \quad (12)$$

where \mathbf{n}_{Γ} is the outward normal to $\Gamma_{\mathbf{x}}$. This means that the outgoing flux is based on the cell internal quantity $f(\mathbf{x}, \vartheta)$, and the incoming flux is based on some external quantity $\tilde{f}(\mathbf{x}, \vartheta)$.

In order to discretize the system in space and angles, the space may be shrunk to a finite basis. It is convenient to define two different bases. First, the finite basis for the transported quantity $f(\mathbf{x}, \vartheta)$

$$\Psi = \omega \otimes \psi = [\omega_1(\vartheta) \psi_1(\mathbf{x}), \dots, \omega_1(\vartheta) \psi_N(\mathbf{x}), \dots, \omega_M(\vartheta) \psi_1(\mathbf{x}), \dots, \omega_M(\vartheta) \psi_N(\mathbf{x})]^T, \quad (13)$$

and second, the finite basis for the source term $S(\mathbf{x}, \vartheta)$

$$\Phi = \omega \otimes \phi = [\omega_1(\vartheta) \phi_1(\mathbf{x}), \dots, \omega_1(\vartheta) \phi_{\tilde{N}}(\mathbf{x}), \dots, \omega_M(\vartheta) \phi_1(\mathbf{x}), \dots, \omega_M(\vartheta) \phi_{\tilde{N}}(\mathbf{x})]^T, \quad (14)$$

where \otimes is the outer tensor product. The use of the tensor product allows us to work with a separate basis ω for the angular part and a separate basis ψ or ϕ for the spatial part, that is,

$$\omega = [\omega_1(\vartheta), \dots, \omega_M(\vartheta)]^T, \quad \psi = [\psi_1(\mathbf{x}), \dots, \psi_N(\mathbf{x})]^T, \quad \phi = [\phi_1(\mathbf{x}), \dots, \phi_{\tilde{N}}(\mathbf{x})]^T. \quad (15)$$

This is the definition of discrete spaces H_{Ψ} and H_{Φ} , where we can find the following discrete representation (degrees of freedom) of the distribution and source functions

$$\mathbf{f} = [\mathbf{f}_1, \dots, \mathbf{f}_{M \cdot N}]^T, \quad (16)$$

$$\mathbf{S} = [\mathbf{S}_1, \dots, \mathbf{S}_{M \cdot \tilde{N}}]^T, \quad (17)$$

and their spatial and angular evaluation

$$f(\mathbf{x}, \vartheta) = \Psi(\mathbf{x}, \vartheta)^T \cdot \mathbf{f}, \quad (18)$$

$$S(\mathbf{x}, \vartheta) = \Phi(\mathbf{x}, \vartheta)^T \cdot \mathbf{S}. \quad (19)$$

The reason for using a different spatial basis in the case of source $S(\mathbf{x}, \vartheta)$ proves to be useful in numerical tests in Section 4. A similar need of using different basis for thermodynamic quantities (pressure) and transport quantities (flux of momentum) was addressed and theoretically studied in the Stokes flux problem [13]. Because we solve the coupled system of temperature T and transport of energy, we can see that our problem resembles the Stokes problem, while flux (6) is based on $f(\mathbf{x}, \vartheta)$ and thermodynamic quantity is represented by $S(\mathbf{x}, \vartheta)$, which is spatially distributed as thermodynamic quantity (temperature) (8). In general, one can apply a different basis in angular space as well.

Based on the previous discretization (18, 19), we can formulate a system of equations of the unknown \mathbf{f} , the discrete representation of the distribution function (18), which is dependent on the discrete source \mathbf{S} (19) as follows:

$$\begin{aligned} & \int_{\Omega_\vartheta} \int_{\Omega_x} \Psi \otimes \left(\Psi^T \cdot \frac{1}{c_p} \frac{\partial \mathbf{f}}{\partial t} + \mathbf{n}(\vartheta) \cdot \nabla \Psi^T \cdot \mathbf{f} + k_p(\mathbf{x}) \Psi^T \cdot \mathbf{f} - \Phi^T \cdot \mathbf{S} \right) d\Omega_x d\Omega_\vartheta \\ &= \int_{\Omega_\vartheta} \int_{\mathbf{n} \cdot \mathbf{n}_\Gamma < 0} \Psi \otimes \left(\Psi^T \cdot \mathbf{f} - \tilde{\Psi}^T \cdot \tilde{\mathbf{f}} \right) \mathbf{n}(\vartheta) \cdot \mathbf{n}_\Gamma(\mathbf{x}) d\Gamma d\Omega_\vartheta. \end{aligned} \quad (20)$$

The scheme can be written using matrices and the backward Euler implicit method as

$$\begin{aligned} & \frac{1}{c_p} \mathbf{M}^{\Psi\Psi} \cdot \frac{\mathbf{f}^{n+1} - \mathbf{f}^n}{\Delta t} + \mathbf{D}^{\Psi\Psi} \cdot \mathbf{f}^{n+1} + k_p(\mathbf{x}) \mathbf{M}^{\Psi\Psi} \cdot \mathbf{f}^{n+1} - \mathbf{M}^{\Psi\Phi} \cdot \mathbf{S}^{n+1} \\ &= \mathbf{\Gamma}^{\Psi\Psi-} \cdot \mathbf{f}^{n+1} - \tilde{\mathbf{\Gamma}}^{\Psi\tilde{\Psi}} \cdot \tilde{\mathbf{f}}, \end{aligned} \quad (21)$$

where the basis functions matrices being used are the following:

$$\mathbf{M}^{\Psi\Psi} = \int_{\Omega_\vartheta} \omega \otimes \omega^T d\Omega_\vartheta \otimes \int_{\Omega_x} \psi \otimes \psi^T d\Omega_x, \quad (22)$$

$$\mathbf{D}^{\Psi\Psi} = \int_{\Omega_\vartheta} \omega \otimes \omega^T \mathbf{n}_i d\Omega_\vartheta \otimes \int_{\Omega_x} \psi \otimes \frac{\partial \psi^T}{\partial x_i} d\Omega_x, \quad (23)$$

$$\mathbf{\Gamma}^{\Psi\Psi-} = \int_{\Omega_\vartheta} \int_{\mathbf{n} \cdot \mathbf{n}_\Gamma < 0} (\omega \otimes \omega^T) \otimes (\psi \otimes \psi^T) \mathbf{n}(\vartheta) \cdot \mathbf{n}_\Gamma(\mathbf{x}) d\Gamma d\Omega_\vartheta, \quad (24)$$

$$\tilde{\mathbf{\Gamma}}^{\Psi\tilde{\Psi}} = \int_{\Omega_\vartheta} \int_{\mathbf{n} \cdot \mathbf{n}_\Gamma < 0} (\omega \otimes \tilde{\omega}^T) \otimes (\psi \otimes \tilde{\psi}^T) \mathbf{n}(\vartheta) \cdot \mathbf{n}_\Gamma(\mathbf{x}) d\Gamma d\Omega_\vartheta, \quad (25)$$

$$\mathbf{M}^{\Psi\Phi} = \int_{\Omega_\vartheta} \omega \otimes \omega^T d\Omega_\vartheta \otimes \int_{\Omega_x} \psi \otimes \phi^T d\Omega_x, \quad (26)$$

where summation over the index i , that is, spatial dimensions, has been performed in the case of the divergence matrix $\mathbf{D}^{\Psi\Psi}$. Finally, we write the discrete solution to (9) in the compact form

$$\begin{aligned} & \left(\left(\frac{1}{c_p \Delta t} + k_p \right) \mathbf{M}^{\Psi\Psi} + \mathbf{D}^{\Psi\Psi} - \mathbf{\Gamma}^{\Psi\Psi-} \right) \cdot \mathbf{f}^{n+1} \\ &= \mathbf{M}^{\Psi\Phi} \cdot \mathbf{S}^{n+1} + \frac{1}{c_p \Delta t} \mathbf{M}^{\Psi\Psi} \cdot \mathbf{f}^n - \tilde{\mathbf{\Gamma}}^{\Psi\tilde{\Psi}} \cdot \tilde{\mathbf{f}}. \end{aligned} \quad (27)$$

Because we are particularly interested in the explicit dependence of $f(\mathbf{x}, \boldsymbol{\vartheta})$, or better, the dependence of discrete representation \mathbf{f}^{n+1} on temperature, we can, in general, write the temperature dependent source

$$\mathbf{S}^{n+1} = \mathbf{S}_{\Omega_{\boldsymbol{\vartheta}\mathbf{x}}}^p \cdot \mathbf{T}^{n+1} + \mathbf{h}_{\Omega_{\boldsymbol{\vartheta}\mathbf{x}}}^p, \quad (28)$$

that is, a linear dependence of source on a discrete temperature vector \mathbf{T}^{n+1} being from H_{Φ} . In [14, 15] the same idea of discretizing the transport flux as a function of temperature was proposed. The indexes p and $\Omega_{\boldsymbol{\vartheta}\mathbf{x}}$ refer to the spatial discretization on $\Omega_{\mathbf{x}}$, the angular discretization on $\Omega_{\boldsymbol{\vartheta}}$, and the energy discretization p . When using (28) in (27), we obtain a linear dependence of the unknown distribution function on temperature as

$$\left(\mathbf{f}_{\Omega_{\boldsymbol{\vartheta}\mathbf{x}}}^p\right)^{n+1} = \mathbf{A}_{\Omega_{\boldsymbol{\vartheta}\mathbf{x}}}^p \cdot \mathbf{T}^{n+1} + \mathbf{b}_{\Omega_{\boldsymbol{\vartheta}\mathbf{x}}}^p, \quad (29)$$

where the explicit formulas of the solution coefficients are

$$\mathbf{L} = \left(\left(\frac{1}{c_p \Delta t} + k_p \right) \mathbf{M}^{\Psi\Psi} + \mathbf{D}^{\Psi\Psi} - \mathbf{\Gamma}^{\Psi\Psi} \right), \quad (30)$$

$$\mathbf{A}_{\Omega_{\boldsymbol{\vartheta}\mathbf{x}}}^p = \mathbf{L}^{-1} \cdot \mathbf{M}^{\Psi\Phi} \cdot \mathbf{S}_{\Omega_{\boldsymbol{\vartheta}\mathbf{x}}}^p, \quad (31)$$

$$\mathbf{b}_{\Omega_{\boldsymbol{\vartheta}\mathbf{x}}}^p = \mathbf{L}^{-1} \cdot \left(\frac{1}{c_p \Delta t} \mathbf{M}^{\Psi\Psi} \cdot \mathbf{f}^n - \tilde{\mathbf{\Gamma}}^{\Psi\Psi} \cdot \tilde{\mathbf{f}} + \mathbf{M}^{\Psi\Phi} \cdot \mathbf{h}_{\Omega_{\boldsymbol{\vartheta}\mathbf{x}}}^p \right). \quad (32)$$

The use of (29) is the following: we discretize the phase space of $f(\mathbf{x}, \boldsymbol{\vartheta})$, that is, by applying a spatial mesh, in general 3D, and an angular plus energy discretization, that is, the momentum space will always be represented in spherical coordinates $\boldsymbol{\vartheta} = (\theta, \varphi)$ and p being the momentum norm. We can use (29) to evolve the distribution function $\mathbf{f}_{\Omega_{\boldsymbol{\vartheta}\mathbf{x}}}^p$ on a given cell ($\Omega_{\mathbf{x}}$), a given range of directions ($\Omega_{\boldsymbol{\vartheta}}$) and a given range of energies (p) when the temperature \mathbf{T} has been provided. Technically, the computational sequence consists of construction of (30, 31, 32) on each computational cell separately, which is advantageous for possible parallelization of the scheme. Also, the matrix inversion is not excessively painful, because the size of the matrix reflects the number of degrees of freedom of one element, which is a small number.

3.2. Discontinuous Galerkin temperature scheme

The equation of specific internal energy (3) naturally depends on temperature. We define its simplified form

$$a \frac{\partial T}{\partial t} + \int_p \int_{4\pi} \frac{1}{c_p} \frac{\partial f(\mathbf{x}, \boldsymbol{\vartheta})}{\partial t} + \mathbf{n}(\boldsymbol{\vartheta}) \cdot \nabla f(\mathbf{x}, \boldsymbol{\vartheta}) d\boldsymbol{\vartheta} dp = W(\mathbf{x}), \quad (33)$$

where the integration over the momentum space is written in spherical coordinates, that is, transport direction $\boldsymbol{\vartheta} = (\theta, \varphi)$, the azimuthal and polar angles, respectively, and p being the momentum magnitude. The term W comprises all the terms, which are not related to the nonlocal transport, for example, inverse bremsstrahlung heating, specific internal energy change due to density evolution, work performed by hydrodynamic motion, and electronic heat flux. The spatial discretization of (33) requires high-order method due to the diffusion behavior of transport in the case of short mean free path, that is, the heat equation model [3]. We apply the Galerkin variational principle to (33) leading to

$$\begin{aligned} & \int_{\Omega_{\mathbf{x}}} \phi(\mathbf{x}) \left(a \frac{\partial T}{\partial t} + \int_p \sum_{\Omega_{\boldsymbol{\vartheta}}} \left[\int_{\Omega_{\boldsymbol{\vartheta}}} \left(\frac{1}{c_p} \frac{\partial f(\mathbf{x}, \boldsymbol{\vartheta})}{\partial t} + \mathbf{n}(\boldsymbol{\vartheta}) \cdot \nabla f(\mathbf{x}, \boldsymbol{\vartheta}) \right) d\Omega_{\boldsymbol{\vartheta}} \right] dp - W(\mathbf{x}) \right) d\Omega_{\mathbf{x}} \\ & = 0, \forall \phi \in H(\Omega_{\mathbf{x}}). \end{aligned} \quad (34)$$

One should note that the angular coordinates ϑ describe all possible directions of the transported particles, that is, the sum over Ω_{ϑ} must cover all 4π angles. The corresponding transport velocity c_p is related to the particles energy. Discretization of (35) is performed by making use of the spatial basis ϕ of (15). Application of the backward Euler implicit method then yields the scheme

$$\mathbf{M}^{\phi\phi} \cdot \frac{\mathbf{T}^{n+1} - \mathbf{T}^n}{\Delta t} + \sum_p \left[\sum_{\Omega_{\vartheta}} \left(\frac{1}{c_p} \tilde{\mathbf{M}}_{\Omega_{\vartheta}}^{\phi\Psi} \cdot \frac{\mathbf{f}^{n+1} - \mathbf{f}^n}{\Delta t} + \tilde{\mathbf{D}}_{\Omega_{\vartheta}}^{\phi\Psi} \cdot \mathbf{f}^{n+1} \right) \right] \Delta p = \mathbf{M}^{\phi\phi} \cdot \mathbf{W}, \quad (35)$$

where Δp is the energy group range, and its matrices are defined as follows:

$$\mathbf{M}^{\phi\phi} = \int_{\Omega_x} \phi \otimes \phi^T d\Omega_x, \quad (36)$$

$$\tilde{\mathbf{M}}_{\Omega_{\vartheta}}^{\phi\Psi} = \int_{\Omega_{\vartheta}} \omega^T d\Omega_{\vartheta} \otimes \int_{\Omega_x} \phi \otimes \psi^T d\Omega_x, \quad (37)$$

$$\tilde{\mathbf{D}}_{\Omega_{\vartheta}}^{\phi\Psi} = \int_{\Omega_{\vartheta}} \omega^T \mathbf{n}_i(\vartheta) d\Omega_{\vartheta} \otimes \int_{\Omega_x} \phi \otimes \frac{\partial \psi^T}{\partial x_i} d\Omega_x, \quad (38)$$

where \otimes is the outer tensor product. We can further develop the scheme by using (29) for \mathbf{f} , and finally, we obtain the temperature \mathbf{T}^{n+1} variable scheme

$$\begin{aligned} & \left(\frac{a}{\Delta t} \mathbf{M}^{\phi\phi} + \sum_p \left[\sum_{\Omega_{\vartheta}} \left(\frac{1}{c_p \Delta t} \tilde{\mathbf{M}}_{\Omega_{\vartheta}}^{\phi\Psi} + \tilde{\mathbf{D}}_{\Omega_{\vartheta}}^{\phi\Psi} \right) \cdot \mathbf{A}_{\Omega_{\vartheta x}}^p \right] \Delta p \right) \cdot \mathbf{T}^{n+1} = \frac{a}{\Delta t} \mathbf{M}^{\phi\phi} \cdot \mathbf{T}^n \\ & + \mathbf{M}^{\phi\phi} \cdot \mathbf{W} + \sum_p \left[\sum_{\Omega_{\vartheta}} \frac{1}{c_p \Delta t} \tilde{\mathbf{M}}_{\Omega_{\vartheta}}^{\phi\Psi} \cdot \mathbf{f}^n - \left(\frac{1}{c_p \Delta t} \tilde{\mathbf{M}}_{\Omega_{\vartheta}}^{\phi\Psi} + \tilde{\mathbf{D}}_{\Omega_{\vartheta}}^{\phi\Psi} \right) \cdot \mathbf{b}_{\Omega_{\vartheta x}}^p \right] \Delta p. \end{aligned} \quad (39)$$

Let us summarize some interesting properties of the discretization scheme (39), which solves the temperature equation (33) and the transport equation (9) for all discrete directions and energies. It has no explicit dependence on \mathbf{f}^{n+1} . Indeed, time evolution of the transported quantity \mathbf{f} for all directions and energies are inherently included in the scheme due to (29). That is, by evolving the temperature in time, we also implicitly evolve the transported quantity distribution \mathbf{f} . In the computational sequence, this is performed for every cell separately, where the intercell communication is performed by means of $\tilde{\mathbf{f}}$ in (27). The quantity $\tilde{\mathbf{f}}$ then must be iterated until the numerical flux aligns to the natural flux (10) for every two neighboring cells. When this alignment is achieved on the whole computational domain and the quantity W in (33) numerically conserves energy, the discrete scheme (39) of (3) is also conservative in energy. We refer to the number of iterations needed as γ .

3.3. One-dimensional slab geometry case of discontinuous Galerkin Bhatnagar–Gross–Krook transport and temperature scheme

There are several assumptions to simplify the general case of transport in 1D. First, the distribution function is axisymmetric with respect to the 1D axis. In other words, the distribution function depends only on one spatial coordinate, in our case z , and one angular coordinate, in our case polar angle φ , that is, $f(z, \varphi)$. Such a description offers a complete physical model based on symmetries. When modeling the transport problem, we can use the Cartesian coordinate system, and we choose z to be the coordinate along which the functions change. In other words, the spatial basis function is constant along the x and y coordinates. Then, we assume that the representation of the transport directions is given by the polar angle φ only. That is, the angular basis functions do not need to depend on the azimuthal angle θ , that is, they are constant, which is again true for transport in the

1D slab geometry. The scheme is then modified by using a definition of the upwind numerical flux, which depends on the z component only, that is,

$$\mathbf{F}(z, \varphi)^* = \begin{cases} \mathbf{n}(\varphi) f(z, \varphi), & n_z(\varphi) n_\Gamma^z(z) \geq 0, \\ \mathbf{n}(\varphi) \tilde{f}(z, \varphi), & n_z(\varphi) n_\Gamma^z(z) < 0. \end{cases} \quad (40)$$

When using the Cartesian representation $n_z(\varphi) = \cos(\varphi)$, we can write the discrete variational formulation (20) in the following way:

$$\begin{aligned} & \int_{\Delta\varphi} \int_{\Delta z} \Psi \otimes \left(\Psi^T \cdot \frac{1}{c_p} \frac{\partial \mathbf{f}}{\partial t} + \cos(\varphi) \frac{\partial \Psi^T}{\partial z} \cdot \mathbf{f} + k_p \Psi^T \cdot \mathbf{f} - \Phi^T \cdot \mathbf{S} \right) dz \sin(\varphi) d\varphi \\ &= \int_{\Delta\varphi} \int_{\cos(\varphi) n_\Gamma^z < 0} \Psi \otimes \left(\Psi^T \cdot \mathbf{f} - \tilde{\Psi}^T \cdot \tilde{\mathbf{f}} \right) \cos(\varphi) n_\Gamma^z(z) d\Gamma \sin(\varphi) d\varphi. \end{aligned} \quad (41)$$

Then, we can show how to calculate the matrices of (21) for the 1D slab symmetry case

$$\mathbf{M}_{1D}^{\Psi\Psi} = \int_{\Delta\varphi} \boldsymbol{\omega} \otimes \boldsymbol{\omega}^T \sin(\varphi) d\varphi \otimes \int_{\Delta z} \boldsymbol{\psi} \otimes \boldsymbol{\psi}^T dz, \quad (42)$$

$$\mathbf{D}_{1D}^{\Psi\Psi} = \int_{\Delta\varphi} \boldsymbol{\omega} \otimes \boldsymbol{\omega}^T \cos(\varphi) \sin(\varphi) d\varphi \otimes \int_{\Delta z} \boldsymbol{\psi} \otimes \frac{\partial \boldsymbol{\psi}^T}{\partial z} dz, \quad (43)$$

$$\Gamma_{1D}^{\Psi\Psi^-} = \int_{\Delta\varphi} \int_{\cos(\varphi) n_\Gamma^z < 0} (\boldsymbol{\omega} \otimes \boldsymbol{\omega}^T) \otimes (\boldsymbol{\psi} \otimes \boldsymbol{\psi}^T) \cos(\varphi) n_\Gamma^z(z) d\Gamma \sin(\varphi) d\varphi, \quad (44)$$

$$\tilde{\Gamma}_{1D}^{\Psi\Psi} = \int_{\Delta\varphi} \int_{\cos(\varphi) n_\Gamma^z < 0} (\boldsymbol{\omega} \otimes \tilde{\boldsymbol{\omega}}^T) \otimes (\boldsymbol{\psi} \otimes \tilde{\boldsymbol{\psi}}^T) \cos(\varphi) n_\Gamma^z(z) d\Gamma \sin(\varphi) d\varphi, \quad (45)$$

$$\mathbf{M}_{1D}^{\Psi\Phi} = \int_{\Delta\varphi} \boldsymbol{\omega} \otimes \boldsymbol{\omega}^T \sin(\varphi) d\varphi \otimes \int_{\Delta z} \boldsymbol{\psi} \otimes \boldsymbol{\phi}^T dz. \quad (46)$$

The temperature scheme (35) can be expressed in the same manner, and its matrices in the 1D slab geometry are evaluated as

$$\mathbf{M}_{1D}^{\Phi\Phi} = \int_{\Delta z} \boldsymbol{\phi} \otimes \boldsymbol{\phi}^T dz, \quad (47)$$

$$\tilde{\mathbf{M}}_{1D}^{\Phi\Psi} = 2\pi \int_{\Delta\varphi} \boldsymbol{\omega}^T \sin(\varphi) d\varphi \otimes \int_{\Delta z} \boldsymbol{\phi} \otimes \boldsymbol{\psi}^T dz, \quad (48)$$

$$\tilde{\mathbf{D}}_{1D}^{\Phi\Psi} = 2\pi \int_{\Delta\varphi} \boldsymbol{\omega}^T \cos(\varphi) \sin(\varphi) d\varphi \otimes \int_{\Delta z} \boldsymbol{\phi} \otimes \frac{\partial \boldsymbol{\psi}^T}{\partial z} dz, \quad (49)$$

where 2π comes from the integration over θ . The earlier definition of all the matrices is then sufficient to construct the 1D slab geometry DGBGK&T scheme based on transport (29) and on temperature (39) schemes, when the discrete basis $\boldsymbol{\omega}$, $\boldsymbol{\psi}$, and $\boldsymbol{\phi}$ are specified. The simplest transport setting is with angular discretization $\Delta\varphi_1 = (0, \pi/2)$ and $\Delta\varphi_2 = (\pi/2, \pi)$ and one energy group of photons, that is, only two extra unknowns \mathbf{f}_1 and \mathbf{f}_2 emerge apart of \mathbf{T} , where the quantity \mathbf{f} comprises photons of all energies.

4. NUMERICAL TESTS

A numerical scheme itself is a theoretical concept, which aims to be applied to some computations. In order to prepare the DG-BGK&T method to be used in practice, we coded the appropriate parts of the scheme and benchmarked its capabilities on several test cases against the appropriate analytical solutions. In the following text, we are using the notation used in [16, 17], the original work using the MFEM finite element library [18] for Lagrangian hydrodynamics. When using Qn, we refer to the n th order polynomial basis of finite element used for discretization of the intensity I , the unknown of the DG-BGK transport scheme; when using QnQm we refer to the n th-order finite element basis of intensity and m th-order finite element basis used for discretization of the temperature T . For example, we use Q3Q2, which means a bicubic polynomial basis of intensity and biquadratic polynomial basis of temperature. The notation I[Qn] and T[QnQm] then stand for the numerical solution of intensity and temperature using the appropriate discretization. All tests are performed on rectangular quadrilateral finite elements defined on Ω_{xz} . This is a region of the two-dimensional Cartesian coordinate system, that is, a region of the $x - z$ plane, where the finite element matrices of the DG-BGK&T scheme are then evaluated. We show how to calculate the matrices of (21) in the two-dimensional Cartesian case

$$\mathbf{M}_{xz}^{\Psi\Psi} = \int_{\Delta\theta} \int_{\Delta\varphi} \boldsymbol{\omega} \otimes \boldsymbol{\omega}^T \sin(\varphi) d\varphi d\theta \otimes \int_{\Omega_{xz}} \boldsymbol{\psi} \otimes \boldsymbol{\psi}^T dx dz, \quad (50)$$

$$\begin{aligned} \mathbf{D}_{xz}^{\Psi\Psi} &= \int_{\Delta\theta} \int_{\Delta\varphi} \boldsymbol{\omega} \otimes \boldsymbol{\omega}^T \cos(\theta) \sin(\varphi) \sin(\varphi) d\varphi d\theta \otimes \int_{\Omega_{xz}} \boldsymbol{\psi} \otimes \frac{\partial \boldsymbol{\psi}^T}{\partial x} dx dz \\ &+ \int_{\Delta\theta} \int_{\Delta\varphi} \boldsymbol{\omega} \otimes \boldsymbol{\omega}^T \cos(\varphi) \sin(\varphi) d\varphi d\theta \otimes \int_{\Omega_{xz}} \boldsymbol{\psi} \otimes \frac{\partial \boldsymbol{\psi}^T}{\partial z} dx dz, \end{aligned} \quad (51)$$

$$\begin{aligned} \Gamma_{xz}^{\Psi\Psi^-} &= \int_{\Delta\theta} \int_{\Delta\varphi} \int_{\mathbf{n} \cdot \mathbf{n}_\Gamma < 0} (\boldsymbol{\omega} \otimes \boldsymbol{\omega}^T) \otimes (\boldsymbol{\psi} \otimes \boldsymbol{\psi}^T) \\ &(\cos(\theta) \sin(\varphi) n_\Gamma^x(x, z) + \cos(\varphi) n_\Gamma^z(x, z)) d\Gamma_{xz} \sin(\varphi) d\varphi d\theta, \end{aligned} \quad (52)$$

$$\begin{aligned} \tilde{\Gamma}_{xz}^{\Psi\tilde{\Psi}} &= \int_{\Delta\theta} \int_{\Delta\varphi} \int_{\mathbf{n} \cdot \mathbf{n}_\Gamma < 0} (\boldsymbol{\omega} \otimes \tilde{\boldsymbol{\omega}}^T) \otimes (\boldsymbol{\psi} \otimes \tilde{\boldsymbol{\psi}}^T) \\ &(\cos(\theta) \sin(\varphi) n_\Gamma^x(x, z) + \cos(\varphi) n_\Gamma^z(x, z)) d\Gamma_{xz} \sin(\varphi) d\varphi d\theta, \end{aligned} \quad (53)$$

$$\mathbf{M}_{xz}^{\Psi\Phi} = \int_{\Delta\theta} \int_{\Delta\varphi} \boldsymbol{\omega} \otimes \boldsymbol{\omega}^T \sin(\varphi) d\varphi d\theta \otimes \int_{\Omega_{xz}} \boldsymbol{\psi} \otimes \boldsymbol{\phi}^T dx dz, \quad (54)$$

where n_Γ^x and n_Γ^z are the x and z component of the normal to the boundary Γ_{xz} . The temperature scheme (35) is constructed with the help of the following matrices:

$$\mathbf{M}_{xz}^{\Phi\Phi} = \int_{\Omega_{xz}} \boldsymbol{\phi} \otimes \boldsymbol{\phi}^T dx dz, \quad (55)$$

$$\tilde{\mathbf{M}}_{xz}^{\Phi\Psi} = \int_{\Delta\theta} \int_{\Delta\varphi} \boldsymbol{\omega}^T \sin(\varphi) d\varphi d\theta \otimes \int_{\Omega_{xz}} \boldsymbol{\phi} \otimes \boldsymbol{\psi}^T dx dz, \quad (56)$$

$$\begin{aligned} \tilde{\mathbf{D}}_{xz}^{\Phi\Psi} &= \int_{\Delta\theta} \int_{\Delta\varphi} \boldsymbol{\omega}^T \cos(\theta) \sin(\varphi) \sin(\varphi) d\varphi d\theta \otimes \int_{\Omega_{xz}} \boldsymbol{\phi} \otimes \frac{\partial \boldsymbol{\psi}^T}{\partial x} dx dz \\ &+ \int_{\Delta\theta} \int_{\Delta\varphi} \boldsymbol{\omega}^T \cos(\varphi) \sin(\varphi) d\varphi d\theta \otimes \int_{\Omega_{xz}} \boldsymbol{\phi} \otimes \frac{\partial \boldsymbol{\psi}^T}{\partial z} dx dz. \end{aligned} \quad (57)$$

We prefer to use such a simplified transport problem because we can demonstrate numerical properties of the DG-BGK&T method in two dimensions when compared with simplified analytical solutions found as only one direction transport. The simplification resides in that we represent the angular region $\Delta\varphi \times \Delta\theta$ by a constant intensity in a given direction represented by fixed angles, that is, $\mathbf{n}(\varphi_0, \theta_0)$.[‡] The use of the constant intensity representation over the angular region should be clarified. As a useful example, we evaluate the angular part of the x component of the divergence matrix (51) based on a constant basis function, $\boldsymbol{\omega} = [1]^T$ of (15), for the fixed direction $\varphi_0 = \pi/2$, $\theta_0 = 0$ over the angles $\Delta\varphi = (0, \pi)$ and $\Delta\theta = (-\pi/2, \pi/2)$ as

$$\int_{\Delta\theta} \int_{\Delta\varphi} \boldsymbol{\omega} \otimes \boldsymbol{\omega}^T \cos(0) \sin(\pi/2) \sin(\pi/2) d\varphi d\theta = \pi^2. \quad (58)$$

The first test focuses on the transport scheme only, where the temperature-dependent source function is supposed to be static, that is, does not change in time. This brings the advantage that we can find an analytical solution. Furthermore, we can find solutions of any mode of transport, that is, free-streaming, nonlocal, or diffusive. The idea of the second test case is to demonstrate the asymptotic behavior when approaching the diffusive transport limit. According to our knowledge, it is not common for transport numerical schemes to approximate diffusion in an appropriate way. In other words, we want to stress the importance of the higher order scheme for both intensity and temperature because with low-order scheme, the diffusive heat conduction is not recovered.

4.1. Exact steady transport test of discontinuous Galerkin Bhatnagar–Gross–Krook scheme

The slab geometry implies that the source function and the boundary condition depend only on one coordinate; in our case, on z coordinate. We define $\mu = \cos(\Theta)$ where Θ is an angle between the intensity direction \mathbf{n} and z -axis. We apply the zero boundary condition, that is, $I(z_0, \mu) = 0$ and the steady state is represented by $\frac{\partial I}{\partial t} = 0$. Consequently, we obtain a simplified form of (9), an ordinary differential equation [19]

$$\mu \frac{dI(z, \mu)}{dz} = k (f(z) - I(z, \mu)), \quad (59)$$

where the constant $k = \lambda^{-1}$ is the inverse of the particle mean free path, also called absorptivity, and $f(z)$ is an explicit source function. We can find a formal solution of (59) as [2]

$$I(z, \mu, z_0) = \int_{z_0}^z f(\tilde{z}) \exp\left(\frac{k}{\mu}(\tilde{z} - z)\right) \frac{k}{\mu} d\tilde{z}. \quad (60)$$

In our particular case, we use the source function

$$f(z) = \sin(\pi z), \quad (61)$$

defined on the interval $z \in (0, 1)$. The corresponding solution of (60) reads

$$\begin{aligned} I(z, \mu, z_0) = & \exp\left(\frac{k(z_0 - z)}{\mu}\right) \left(\frac{k\pi\mu \cos(\pi z_0)}{\mu^2\pi^2 + k^2} - \frac{k^2 \sin(\pi z_0)}{\mu^2\pi^2 + k^2} \right) \\ & + \frac{k^2}{\mu^2\pi^2 + k^2} \left(\sin(\pi z) - \frac{\mu\pi}{k} \cos(\pi z) \right). \end{aligned} \quad (62)$$

In order to find a numerical solution of (59) with $\mu = \cos(\pi/4)$, we used the time-dependent DG-BGK scheme (21) described by matrices (50–54). The scheme was evaluated in the direction $\varphi_0 = 3/4\pi$ and $\theta_0 = 0$, corresponding to $\mu = \cos(\pi/4)$, and over the angles $\Delta\varphi = (0, \pi)$ and $\Delta\theta = (-\pi/2, \pi/2)$ according to (58). The scheme had been iterated until the steady solution was

[‡]The constant intensity representation is achieved by using a one-point quadrature rule in the point (φ_0, θ_0) . The scheme matrices (50–57) are so evaluated by using the MFEM library [18].

obtained. The iteration was stopped when the relative change of the L1 norm of I was less than 10^{-15} . Figure 1 shows the results calculated using the quadrilateral element Q3. The intensity I is generated by the source function $\sin(\pi z)$, and photons travel in the direction from left to right. We show three different values of $k = 10^{-4}, 1, 10^4$. One can observe that in the diffusive case, the intensity aligns with the source function $\sin(\pi z)$, which is in agreement with (62) evaluated for $k = 10^4$. Table I shows errors and convergence order of our method. We used the L1 norm errors of computed intensity compared with the analytic solution (62) with $\mu = \cos(\pi/4)$ on a rectangular mesh discretizing the region $(0, 1) \times (0, 1)$ of the $z - x$ plane.

It is shown that our method is high-order accurate for values $k \in (10^{-4}, 10^4)$. This is equivalent to the range of Knudsen number $K_n = \lambda/L \in (10^4, 10^{-4})$ because the characteristic length of the system is $L = 1$, that is, half period of the source function $\sin(\pi z)$. The range of Knudsen

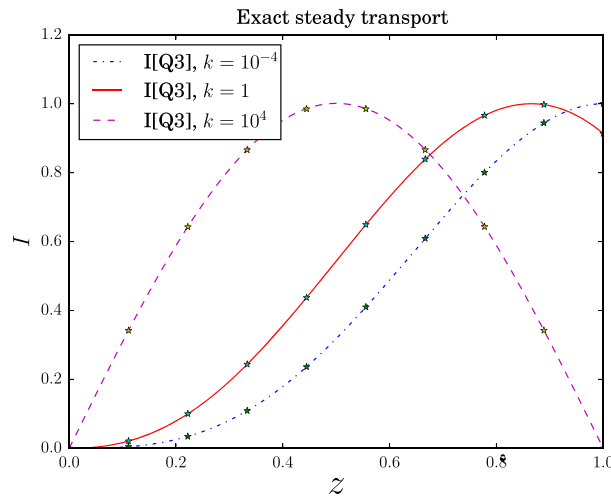


Figure 1. Numerical steady-state solution to (59) calculated using quadrilateral element Q3. Photons are generated by the static source function $\sin(\pi z)$ and travel in the direction from left to right. We show three different values of $k = 10^{-4}, 1, 10^4$, which correspond to free-streaming, nonlocal, and diffusive transport, respectively. The normalized exact solution is represented with lines and corresponding numerical approximation with stars. The maximum value of I in case of $k = 10^{-4}, 1, 10^4$ are $I_{max} = 7.2 \cdot 10^{-9}, 0.51, 1$, respectively. The maximum value reflects the weakness of source function due to small k . Table I shows quantitative errors and convergence order of our method.

Table I. Steady-state test errors and convergence order. Our method proves to be high-order accurate for values $k \in (10^{-4}, 10^4)$ covering transparent, nonlocal, and diffusive transport regimes in plasma.

Element	Cells	$E_{L1}^{k=10^{-4}}$	$q_{L1}^{k=10^{-4}}$	$E_{L1}^{k=1}$	$q_{L1}^{k=1}$	$E_{L1}^{k=10^4}$	$q_{L1}^{k=10^4}$
I[Q1]	10	2.7e-07		2.3e-03	0.0	8.3e-03	
I[Q1]	20	4.9e-08	2.5	4.3e-04	2.4	1.6e-03	2.4
I[Q1]	40	1.2e-08	2.0	1.1e-04	2.0	3.7e-04	2.1
I[Q1]	80	2.9e-09	2.0	2.6e-05	2.0	9.0e-05	2.1
I[Q2]	10	4.6e-09		4.1e-05	0.0	3.5e-07	
I[Q2]	20	4.1e-10	3.5	3.5e-06	3.5	5.2e-08	2.8
I[Q2]	40	4.5e-11	3.2	4.0e-07	3.2	1.2e-08	2.1
I[Q2]	80	5.4e-12	3.1	4.7e-08	3.1	2.8e-09	2.1
I[Q3]	10	7.3e-11		2.6e-07	0.0	2.3e-06	
I[Q3]	20	2.8e-12	4.7	8.4e-09	5.0	1.0e-07	4.5
I[Q3]	40	1.5e-13	4.2	4.3e-10	4.3	5.6e-09	4.2
I[Q3]	80	8.9e-15	4.1	2.4e-11	4.1	3.3e-10	4.1

Our method proves to be high-order accurate for values $k \in (10^{-4}, 10^4)$ covering transparent, nonlocal, and diffusive transport regimes in plasma.

number is large enough to cover conditions of any specific transport, that is, the transparent-like free streaming in the case of $k = 10^{-4}$, the typically nonlocal transport represented by $k = 1$, and the diffusion-like regime corresponding to $k = 10^4$.

We are particularly interested in diffusive condition, that is, when $k \gg 1$. In that case, the first term of (62) behaves as $\exp(-z/\mu k)$ and is immediately damped. The second term tends to $\sin(\pi z) - \frac{\mu\pi}{k} \cos(\pi z)$, which is nothing else than the asymptotic formula $I \approx f - \mu/k \frac{df}{dz}$ corresponding to diffusion of the BGK operator described in [2]. In order to discuss the numerical results, we consider $k = 10^4$. The anisotropic part of (62), that is, the term provoking energy transport, gives approximately

$$-\frac{k^2}{\mu^2 \pi^2 + k^2} \frac{\mu \pi}{k} \cos(\pi z) \approx 1e-4, \quad (63)$$

where $k = 10^4$, $\mu = \cos(\pi/4)$. We can conclude that in the case of the diffusive regime, the second-order element Q1 is not efficient because it gives an error 9.0e-5 on 80 cells spatial resolution, which is of the same order as the diffusive term (63); meanwhile, the error 2.3e-6 on 10 cells spatial resolution obtained by the fourth-order element Q3 is in order of percents of (63), that is, it satisfies the diffusion regime even on such a rough spatial resolution.

4.2. Approximate multigroup diffusion test of discontinuous Galerkin Bhatnagar–Gross–Krook and temperature scheme

The previous numerical test demonstrated that the transport scheme is high-order accurate for any value of absorptivity, that is, it is also consistent with the diffusive asymptotic of the BGK equation (9). This is an extremely important property. The accuracy is not a question of the transport scheme only, it is also crucial that the temperature scheme demonstrates accuracy in the case of diffusion.

One can define a simple model of energy transport. The temperature-dependent source $k\sigma T$, where k^{-1} is the particle mean free path and σ a material constant, generates energetic particles, for example, photons. These are transported with velocity c and reabsorbed within the travel distance of k^{-1} , thus producing a temperature profile evolution due to the energy transport. We also want to represent two groups of energetic particles with different mean free paths k_{g1}^{-1}, k_{g2}^{-1} , where g_j represents an energetic group. By defining a principal direction, or better, two counter-streaming transport directions $\mathbf{n}^+ = -\mathbf{n}^-$, we can write the transport model as a set of equations

$$\frac{1}{c} \frac{\partial I_{g_j}^+}{\partial t} + \mathbf{n}^+ \cdot \nabla I_{g_j}^+ = k_{g_j} (\sigma T - I_{g_j}^+), \quad (64)$$

$$\frac{1}{c} \frac{\partial I_{g_j}^-}{\partial t} + \mathbf{n}^- \cdot \nabla I_{g_j}^- = k_{g_j} (\sigma T - I_{g_j}^-), \quad (65)$$

$$C_v \frac{\partial T}{\partial t} + \pi^2 \sum_{j=1,2} \sum_{i=+,-} \left(\frac{1}{c} \frac{\partial I_{g_j}^i}{\partial t} + \mathbf{n}^i \cdot \nabla I_{g_j}^i \right) \Delta_{g_j} = 0, \quad (66)$$

where two-directional two-group intensities $(I_{g1}^+, I_{g1}^-, I_{g2}^+, I_{g2}^-)$ represent the transported particles, c is speed of light, C_v is the heat capacity, and Δ_g is an energetic group weight.

It is not easy to find an analytic solution to such a self-consistent system. The solution can be found in the case of two asymptotic behaviors $k \rightarrow 0$ and $k \rightarrow \infty$. The solution to the first asymptotic is trivial because there are no particles generated and, consequently, the energy flux is zero. In order to find the solution to the second asymptotic, one way is to apply the Hilbert expansion in a small parameter k^{-1} [7]. This leads to the local approximation of (64, 65) as

$$I_{g_j}^+ = \sigma T - \frac{\sigma}{k_{g_j}} \mathbf{n}^+ \cdot \nabla T + O(k_{g_j}^{-2}) \approx \sigma T - \frac{\sigma}{k_{g_j}} \frac{\partial T}{\partial x}, \quad (67)$$

$$I_{g_j}^- = \sigma T - \frac{\sigma}{k_{g_j}} \mathbf{n}^- \cdot \nabla T + O(k_{g_j}^{-2}) \approx \sigma T + \frac{\sigma}{k_{g_j}} \frac{\partial T}{\partial x}, \quad (68)$$

where we used $\mathbf{n}^+ = [1, 0]$ and $\mathbf{n}^- = [-1, 0]$ in the second equality for the sake of simplicity. When (67, 68) are used in (66), the following model equation arises

$$\left(C_v + \frac{2(\Delta_{g_1} + \Delta_{g_2})\sigma}{c} \right) \frac{\partial T}{\partial t} \approx 2(\Delta_{g_1} k_{g_1}^{-1} + \Delta_{g_2} k_{g_2}^{-1}) \sigma \frac{\partial^2 T}{\partial x^2}, \quad (69)$$

which is the usual local formulation of transport, that is, the heat equation.

In [3], we found the following analytic solution to the linear heat wave equation (69)

$$T(x, t) = \frac{Q}{\sqrt{4\pi\kappa t}} \exp\left(-\frac{x^2}{4\kappa t}\right), \quad (70)$$

where Q is the amount of energy in the system and

$$\kappa = \frac{2(\Delta_{g_1} k_{g_1}^{-1} + \Delta_{g_2} k_{g_2}^{-1})\sigma}{C_v + \frac{2(\Delta_{g_1} + \Delta_{g_2})\sigma}{c}}, \quad (71)$$

is the heat conductivity.

The vector \mathbf{n}^+ corresponds to the fixed direction $\varphi_0 = \pi/2$ and $\theta_0 = 0$, and its opposite \mathbf{n}^- is equal to the fixed direction $\varphi_0 = \pi/2$ and $\theta_0 = \pi$ in spherical coordinates. The scheme (21) is evaluated for the direction \mathbf{n}^+ over the angles $\Delta\varphi = (0, \pi)$ and $\Delta\theta = (-\pi/2, \pi/2)$ and for the direction \mathbf{n}^- over the angles $\Delta\varphi = (0, \pi)$ and $\Delta\theta = (\pi/2, 3\pi/2)$. We expect the transport DG-BGK scheme (21) approximates accurately both directions (67) and (68), that is, the diffusive asymptotic, if $k_{g_1} \approx k_{g_2} \gg 1$. If so, we expect the scheme (35) to bring the numerical solution converging to the solution of (69), that is, the solution (70). In order to test this property, we choose the following simulation parameters:

$$C_v = \sigma = 2.4 \cdot 10^{11}, c = 3 \cdot 10^{10}, Q = 1, \quad (72)$$

and we let the computational domain span the interval $x \in (-1, 1)$. Because we are focused on the multigroup diffusion, we put the following values

$$k_{g_1} = 10^5, k_{g_2} = 1.25 \cdot 10^4, \Delta_{g_1} = 0.16\pi^2, \Delta_{g_2} = 0.02\pi^2, \quad (73)$$

where the group absorptivity k_{g_1} and k_{g_2} meet the diffusive value of the Knudsen number $K_n = \frac{1}{k_{g_j} L} \approx 10^{-5}$, and where $L = 2$ is the computational domain length. It is also worth noting that both groups are of the same importance in the diffusion conductivity (71), because $\Delta_{g_1} k_{g_1}^{-1} = \Delta_{g_2} k_{g_2}^{-1}$.

The computation starts from the analytical solution (70) at time $t_0 = 150$ and evolves till the final time $t_1 = 246$. Tables II and III show results of several high-order approximations. Our analysis has shown that the scheme based on Q1Q1 discretization does not approximate the solution (70). Actually, the solution T[Q1Q1] stays static aligned to the initial solution. This shows that higher order approximation is necessary in order to model diffusive-like transport. In case of higher order schemes, the decreasing error was appropriately reflected by the order of approximation used; except for Q2Q2, which approximates the physical principle of diffusion but does not converge when discretization is refined. This drawback was cured when we improved the discretization order of I ,

Table II. The relative L_1 -error calculated at $t_1 = 246$ of discretizations QnQm to the solution (70) is shown.

Cells	32	64	128	256	512
T[Q1Q1]	2.2e-01 [5]	2.4e-01 (−0.1)	2.3e-01 (0.0)	2.3e-01 (0.0)	2.3e-01 (0.0)
T[Q2Q2]	8.7e-02 [4]	9.5e-02 (−0.1)	9.8e-02 (−0.0)	9.6e-02 (0.0)	9.1e-02 (0.1)
T[Q3Q2]	1.2e-01 [4]	5.7e-02 (1.1)	1.0e-02 (2.5)	1.3e-03 (2.9)	—
T[Q3Q3]	7.6e-02 [4]	4.6e-02 (0.7)	9.8e-03 (2.2)	1.3e-03 (2.9)	—
T[Q4Q4]	2.9e-02 [4]	9.6e-03 (1.6)	1.3e-03 (2.9)	—	—
T[Q5Q5]	2.3e-03 [4]	8.2e-05 (4.8)	—	—	—
T[Q6Q6]	1.7e-04 [4]	—	—	—	—

In the first column, we also present number of iterations $[\gamma]$ of the discontinuous Galerkin Bhatnagar–Gross–Krook and temperature (DG-BGK&T) scheme to converge, and in other columns, we show the rate of convergence (q) of the scheme. We can see that the solutions T[Q1Q1] and T[Q2Q2] do not converge. Any higher order approximation does.

Table III. The absolute L_0 -error calculated at $t_1 = 246$ of discretizations QnQm to the solution (70) is shown.

Cells	32	64	128	256	512
T[Q1Q1]	5.6e-01 [5]	6.1e-01 (−0.1)	6.3e-01 (−0.0)	6.2e-01 (0.0)	6.1e-01 (0.0)
T[Q2Q2]	2.2e-01 [4]	2.7e-01 (−0.3)	2.8e-01 (−0.1)	2.8e-01 (0.0)	2.6e-01 (0.1)
T[Q3Q2]	2.7e-01 [4]	1.4e-01 (1.0)	2.5e-02 (2.5)	3.2e-03 (3.0)	—
T[Q3Q3]	1.9e-01 [4]	1.3e-01 (0.6)	2.8e-02 (2.2)	3.9e-03 (2.9)	—
T[Q4Q4]	7.5e-02 [4]	2.6e-02 (1.6)	3.6e-03 (2.8)	—	—
T[Q5Q5]	5.5e-03 [4]	2.3e-04 (4.6)	—	—	—
T[Q6Q6]	4.1e-04 [4]	—	—	—	—

In the first column, we also present number of iterations $[\gamma]$ of the discontinuous Galerkin Bhatnagar–Gross–Krook and temperature (DG-BGK&T) scheme to converge, and in other columns, we show the rate of convergence (q) of the scheme. We can see that the solutions T[Q1Q1] and T[Q2Q2] do not converge. Any higher order approximation does.

that is, we used the discretization Q3Q2, which performs better than Q2Q2. It is also worth noting that we have encountered an interesting behavior of the scheme, which is that the combinations Q(n+1)Qn seem to be more stable in simulations. A similar behavior was observed in [20], which will serve as a basis for our future analysis.

The evolution of the solution (70) from the time $t_0 = 150$ to the time $t_1 = 246$ can be found in Figure 2. The numerical solution of the approximation Q3Q2 clearly outperforms the approximation Q2Q2 and provides a reasonable accuracy for 128 cells discretization.

One should be aware that our DG-BGK&T scheme does not use any kind of diffusion operator, that is, it uses the model equations (64, 65, 66). Still, the relative errors in Tables II and III prove the scheme is precisely accurate.

5. SIMULATION OF INTENSE LASER INTERACTION WITH A FOIL TARGET

We describe the numerical method applied for solving the energy transport and energy conservation in the model of plasma heated by laser presented in Section 2. We are particularly interested in the equation of energy conservation (3), which when written in a way similar to (33), reads as follows:

$$\rho \frac{\partial \epsilon}{\partial T} \frac{dT}{dt} + \int_{4\pi} \frac{1}{c} \frac{d\bar{I}}{dt} + \mathbf{n} \cdot \nabla \bar{I} d\mathbf{n} = \left(\rho^2 \frac{\partial \epsilon}{\partial \rho} - p \right) \nabla \cdot \mathbf{u} - \nabla \cdot \mathbf{q}_H + Q_{IB}, \quad (74)$$

where c is speed of light and the quantity of transported photons is described through the frequency averaged intensity $\bar{I}(\mathbf{n})$, which depends on the transport direction \mathbf{n} . This means we are using a one-energy-group of photons approach. The transport equation (8) then simplifies to the form

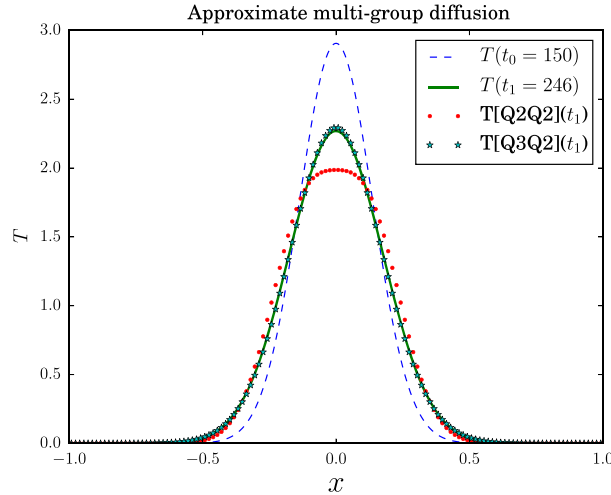


Figure 2. We present the exact solution (70) to the linear heat wave equation (66) in the initial time $t_0 = 150$ (blue dashed line) and in the final time $t_1 = 246$ (green continuous line). Numerical solutions T[Q2Q2] and T[Q3Q2] are figured using red dots and green stars, respectively. It can be seen that the discretization Q3Q2 performs much better than the discretization Q2Q2, which is also demonstrated in Tables II and III.

$$\frac{1}{c} \frac{d\bar{I}}{dt} + \mathbf{n} \cdot \nabla \bar{I} = \rho \kappa (\sigma T^4 - \bar{I}), \quad (75)$$

where ρ is the plasma density, κ is the mean Planck opacity, and σ the Stefan–Boltzmann constant. The heat capacity and the external source term

$$a = \rho \frac{\partial \epsilon}{\partial T}, \quad W = \left(\rho^2 \frac{\partial \epsilon}{\partial \rho} - p \right) \nabla \cdot \mathbf{u} - \nabla \cdot \mathbf{q}_H + Q_{IB}, \quad (76)$$

and the absorptivity and the photon source

$$k_p = \rho \kappa, \quad (77)$$

$$S = \rho \kappa \sigma T^4, \quad (78)$$

are defined with reference to models (33) and (9). We use the gray-body approximation [1] form of the photon source (78).

We describe the experimental situation when Gaussian pulse of full width half maximum duration 300 ps of laser radiation of wavelength $\lambda = 800$ nm and maximum intensity $2 \cdot 10^{14} \text{ W cm}^{-2}$ is incident normally on 5- μm -thick copper foil. In the one-energy group approach, we use the mean Planck opacity of copper

$$\kappa = 2.3 \cdot 10^8 \rho^{0.35} / T^{2.12}, \quad (79)$$

presented in [4], where ρ in $[\text{g cm}^{-3}]$ and T in $[\text{eV}]$.

We have implemented the radiation transport closure model (75) into 1D Lagrangian hydro code based on the methods presented in [21, 22], where we use the 1D DG-BGK&T scheme presented in Section 3.3. The spatial cell distribution comes from the Lagrangian mesh, where explicit contribution of the hydrodynamic compression to the energy reads

$$\rho_i^n \frac{\varepsilon_i^{n+1} - \varepsilon_i^n}{\Delta t} = -p_i \frac{\frac{u_{i+1}^{n+1} + u_{i+1}^n}{2} - \frac{u_i^{n+1} + u_i^n}{2}}{\Delta z_i} \approx -p \nabla \cdot \mathbf{u}. \quad (80)$$

This discrete form of the fluid energy equation of the scheme [22] conserves energy and the term on the right-hand side of (80) enters into our DG-BGK&T scheme as the hydrodynamic contribution of W (76). In the radiation hydrodynamics model (1, 2, 3), we use the equation of state based on SESAME tables [23] to close the system. We present results obtained from the simulation with the following parameters: we used 300 cells mesh with the geometric factor $q = 0.99$. The cell mass decreases when approaching the interaction surface of the target. The laser comes from right to left in duration of 1 ns. In Figure 3, we present the calculated spatial profiles of plasma parameters at the time of 1 ns corresponding to the moment when the maximum of laser pulse interacts with the target. In order to test our DG-BGK&T method, we ran the simulations with discretizations Q1Q1, Q3Q2, and Q5Q5. When comparing the results, we have found that all the discretizations give quantitatively the same numbers. In the case of Q3Q2 and Q5Q5, the results are essentially the same. A noticeable difference shows the mean iteration number commented on in Section 3.2, where we have obtained $\bar{\gamma} = 18, 10, 10$ in the case of Q1Q1, Q3Q2, and Q5Q5, respectively. Consequently, the run times of Q1Q1 and Q3Q2 were practically the same. As a result, it is recommendable to use Q3Q2 discretization.

In the simulation, the total energy radiated out of the plasma is approximately 50% of the absorbed laser energy, and thus, radiation transport is of great importance. The detail of the spatial profiles shown in the left panel of Figure 3 displays the region where the radiation transport is essential for ablation of the target. In this relatively dense but not very hot region, a smooth density gradient is accompanied by a radiation heat wave.

In Section 1, we described an important characterization of radiation transport according to the Knudsen number. Figure 3 provides us sufficient information to analyze the regime of transport in the case of intense-laser interaction with a copper target. We used the Knudsen number definition $K_n = \lambda_p / L$, where λ_p is the inverse of (77), and L is evaluated with respect to the inhomogeneity of the source function S (78). Using the explicit evaluation of S , according to profiles of temperature and density shown in Figure 3, and the Planck opacity (79), we defined the inhomogeneity scale length $L = \Delta z$ from the relation

$$|S(z_0 + \Delta z) - S(z_0)| = \alpha S(z_0), \quad (81)$$

where we used a 10% change, that is, $\alpha = 0.1$. We also evaluated L while using $\alpha \in (0.1, 0.5)$, but the Knudsen number shown in Figure 4 was not changing quantitatively. In Figure 4, we see that the entire domain, where the radiation flux \mathbf{q}_R is quantitatively important, can be classified as nonlocal transport because the Knudsen number spans the interval $K_n \in (10^{-3}, 10^2)$. Especially interesting is the area shown in the left panel of Figure 3 ranging in $K_n \in (10^{-3}, 10^{-1})$, which should be approaching the diffusive regime, at least according to the Knudsen number. Nevertheless, the values of I_0 and I_1 demonstrated in the left panel of Figure 5 differ significantly, and thus, the

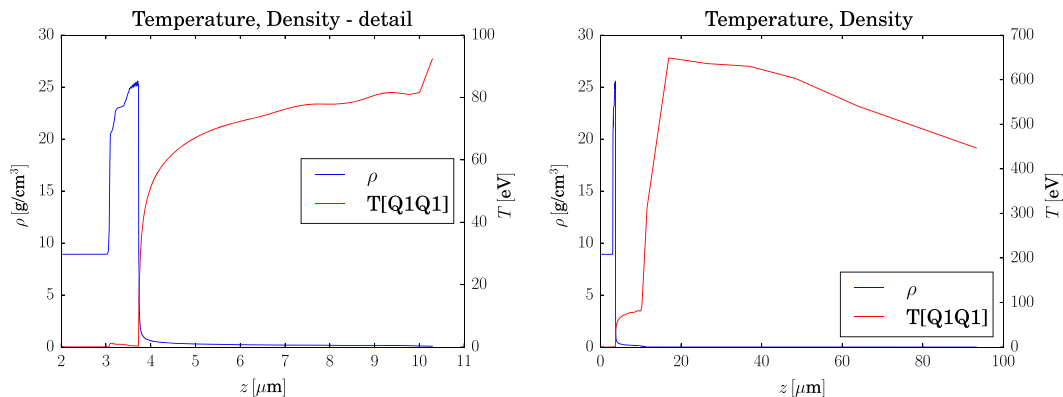


Figure 3. Temperature $T[\text{Q1Q1}]$ and density ρ profiles at the time $t = 1$ ns are shown in the right panel. In the left panel, the detail of the ablation region followed by the shock wave are shown. The laser pulse comes from right to left.

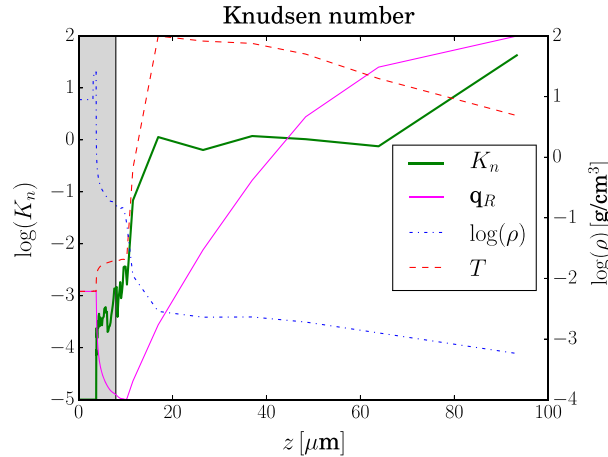


Figure 4. Based on the temperature and density profiles we calculated the Knudsen number K_n . Its logarithm is shown with the thick green line, accompanied by radiation flux \mathbf{q}_R in magenta line, temperature T in dashed red line, and logarithm of density ρ in dashed-dot blue line. The gray vertical span determines the diffusive transport region according to the definition in Section 1.

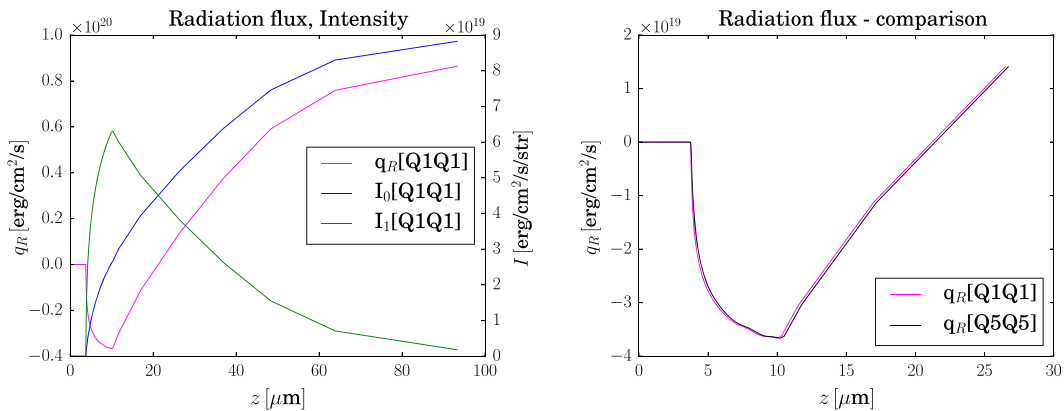


Figure 5. Radiation flux \mathbf{q}_R and photon intensities I_0 and I_1 are shown in the left panel. I_0 represents photons propagating from left to right, and I_1 represents photons propagating from right to left. The figure in the right panel shows the radiation flux \mathbf{q}_R calculated using discretizations Q1Q1 and Q5Q5. One can observe that the difference of these is negligible.

diffusive approximation is not valid for the radiation transport. If the transport were diffusive, the values of I_0 and I_1 would differ only a little, that is, by the first term of expansion as it is in the diffusion condition (67, 68).

The simulation results, especially characterized by Figure 4, point out the importance of the nonlocal transport description in the intense-laser heated plasma because the transport regime deviates from the region of validity of the expansion method of Chapman–Enskog. The right panel of Figure 5 shows that in the case of high-order discretization $\mathbf{q}_R[\text{Q5Q5}]$, the radiation flux exhibits a minor change when compared with the lowest discretization $\mathbf{q}_R[\text{Q1Q1}]$. This should not be the case as is demonstrated in Section 4.2, more precisely in Table II. If the pure diffusive transport had been important, the high-order method would have given different results.

Our results confirm that the directional radiation transport equation closure provides physically relevant results, when the laser-heated plasma is the subject of study. According to [24, 25], the approximate methods based on the first-order spherical harmonics expansion [9] work well when close to the diffusion regime. It would be interesting to challenge these methods with the conditions of laser-heated plasma and compare the results with our method.

6. CONCLUSIONS

Numerical results manifest the capability of the DG-BGK&T method to solve appropriately the transport problem under any Knudsen number condition. The numerical tests show that our method works well in all transport regimes: free-streaming, nonlocal transport, and diffusive regime. We have discovered that the diffusion regime requires the scheme to be of higher order to correctly approximate the solution to the heat wave equation. As far as we know, nobody has used a similar approximate multigroup diffusion test before. We have tried to explore why this behavior occurs by analyzing the small parameter expansion of our DG-BGK&T, but the results we obtained need some more profound theoretical representation. Nevertheless, we have some ideas why the $Q(n+1)Q_n$ scheme performs best with reference to the stability condition of the well studied element Q2P1.

The implicit coupling of photon intensity to plasma temperature proves to be efficient even when used in hydrodynamics simulations of intense laser-heated plasmas. Furthermore, we are quite pleased by the simulation results using the radiation transport closure because the physical phenomena of radiative cooling and smooth plasma ablation seem to be modeled in a reasonable way. When analyzing the Knudsen number of the plasma generated in the laser-target interaction, we have encountered that the transport of energy almost never enters the diffusive regime. This behavior should be analyzed also in case of different materials or experimental settings. Nevertheless, we may say, that the use of Chapman–Enskog expansion method in laser-heated plasma is rather questionable. This property should be further studied.

ACKNOWLEDGEMENTS

Partial support by the project ELI – Extreme Light Infrastructure phase 2 (CZ.02.1.01/0.0/0.0/15 008/0000162) from European Regional Development Fund, by the Ministry of Education, Youth and Sports of the Czech Republic projects LD14089 and RVO 68407700, and by the Czech Technical University project SGS16/247/OHK4/3T/14 is gratefully acknowledged.

REFERENCES

1. Mihalas D, Mihalas BW. *Foundations of Radiation Hydrodynamics*. Oxford University Press: New York, 1985.
2. Castor J. *Radiation Hydrodynamics*. Cambridge University Press: Cambridge, 2004.
3. Zeldovich Y, Raizer Y. *Physics of shock waves and high-temperature hydrodynamic phenomena*. Dover Publications, Inc: New York, 2002.
4. Atzeni S, Meyer-Ter-Vehn J. *The Physics of Inertial Fusion*. Clarendon Press-Oxford: Oxford, 2004.
5. Bhatnagar PL, Gross EP, Krook M. A model for collision processes in gases. I. Small amplitude processes in charged and neutral one-component systems. *Physical Review* 1954; **94**:511–525.
6. Brantov AV, Bychenkov VY. Nonlocal transport in hot plasma. part I. *Plasma Physics Reports* 2013; **39**:698–744.
7. Chapman S, Cowling TG. *Mathematical Theory of Nonuniform Gases*. Cambridge University Press: Cambridge, 1952.
8. L Spitzer J, Harm R. Transport phenomena in a completely ionized gas. *Physical Review* 1953; **89**:977–981.
9. Olson GL, Auer LH, Hall ML. Diffusion, P1, and other approximate forms of radiation transport. *Journal of Quantitative Spectroscopy & Radiative Transfer* 2000; **64**:619–634.
10. Vilar F, Maire PH, Abgrall R. Cell-centered discontinuous Galerkin discretizations for two-dimensional scalar conservation laws on unstructured grids and for one-dimensional Lagrangian hydrodynamics. *Computer and Fluids* 2011; **46**:498–504.
11. Sanchez R, Ragusa J. On the construction of Galerkin angular quadratures. *Nuclear Science and Engineering* 2011; **169**:133–154.
12. Wang Y, Ragusa JC. A high-order discontinuous Galerkin method for the SN transport equations on 2D unstructured triangular meshes. *Annals of Nuclear Energy* 2009; **36**:931–939.
13. Arnold D, Boffi D, Falk R. Approximation by quadrilateral finite elements. *Mathematics Computation* 2002; **71**:909–922.
14. Livne E, Glasner A. A finite difference scheme for the heat conduction equation. *Journal of Computational Physics* 1985; **58**:59–66.
15. Holec M, Cotel M, Velarde P, Liska R. Application of Discontinuous Galerkin Adaptive Mesh and Order Refinement Method to Energy Transport and Conservation Equations in Radiation-Hydrodynamics. In *1st Pan American Congress on Computational Mechanics, Buenos Aires*, Idelsohn SR, Sonzogni V, Coutinho A, Cruchaga M, Lew A, Cerrolaza M (eds). CIMNE: Barcelona, 2015; 919–930.

16. Dobrev V, Kolev T, Rieben R. High-order curvilinear finite element methods for Lagrangian hydrodynamics. *SIAM Journal on Scientific Computing* 2012; **34**:606–641.
17. Dobrev VA, Ellis TE, Kolev TV, Rieben RN. Curvilinear finite elements for Lagrangian hydrodynamics. *International Journal for Numerical Methods in Fluids* 2010; **65**:1295–1310.
18. Kolev T, Dobrev V, Rieben R. MFEM: Modular finite element methods. mfem.org.
19. Basko M, Maruhn J, Tauschwitz A. Development of a 2D radiation-hydrodynamics code RALEF for laser plasma simulations. *Technical Report PLASMA-PHYSICS-25*, EMMI, GSI Darmstadt: Germany, 2009.
20. Boffi D, Gastaldi L. On the quadrilateral Q2-P1 element for the Stokes problem. *International Journal for Numerical Methods* 2002; **39**:1001–1011.
21. Shashkov M, Steinberg S. Solving diffusion equations with rough coefficients in rough grids. *Journal of Computational Physics* 1996; **129**:383–405.
22. Shashkov M. *Conservative Finite-difference Methods on General Grids*. CRC Press: Boca Raton, 1996.
23. Lyon SP, Johnson JD. SESAME: the Los Alamos National Laboratory equation of state database. *Technical Report LA-UR-92-3407*, Los Alamos Scientific Laboratory: Los Alamos, 1992.
24. Morel JE. Diffusion-limit asymptotics of the transport equation, the P1/3 equations, and two flux-limited diffusion theories. *Journal of Quantitative Spectroscopy & Radiative Transfer* 2000; **65**:769–778.
25. Buchler JR. Radiation transfer in the fluid frame. *Journal of Quantitative Spectroscopy & Radiative Transfer* 1983; **30**:395–407.